Robust Quantification of Regional Patterns of Migration in Three-Dimensional Cell Culture Models

Chun Kiet Vong
The University of Auckland
Alan Wang
The University of Auckland
Mike Dragunow
The University of Auckland
Thomas I-H Park
The University of Auckland
Vickie Shim (v.shim@auckland.ac.nz)
The University of Auckland https://orcid.org/0000-0002-1680-4287

Research Article

Keywords: Glioblastoma, Cell migration, Finite element analysis, Spheroid assay

Posted Date: June 11th, 2021

DOI: https://doi.org/10.21203/rs.3.rs-573824/v1

Version of Record: A version of this preprint was published at Journal of Medical and Biological Engineering on February 1st, 2022. See the published version at https://doi.org/10.1007/s40846-022-00680-0.

Robust quantification of regional patterns of migration in three-dimensional cell culture models

Chun Kiet Vong, BSc (Hon)[1,2], Alan Wang, PhD[1,2], Mike Dragunow, PhD [2,3], Thomas I-H. Park, PhD[2,3*], Vickie Shim, PhD[1,*]

[1]Auckland Bioengineering Institute, The University of Auckland

[2]Centre for Brain Research, The University of Auckland

[3]Department of Pharmacology, The Faculty of Medical and Health Sciences, The University of Auckland

* Corresponding authors

Thomas I-H. Park (Thomas.park@auckland.ac.nz)

Vickie Shim (v.shim@auckland.ac.nz)

Abstract

Wound healing assays is a common two-dimensional migration model, with the spheroid assay three-dimensional migration model recently emerging as being more representative of in vivo migration behaviours. These models provide insight to the overall migration of cells in response to various factors such as biological, chemotactic and molecular agents. However, currently available analysis techniques for these assays fall short on providing quantifiable means to measure regional migration patterns, , which is essential to allow more robust assessment of drug treatments on cell migration in a chemotactic fashion. Therefore, the aim of this study is to develop a finite element (FE) based pipeline that can objectively quantify regional migration patterns of cells. Here, we report that our FE based approach was able to accurately measure changes in overall migration areas compared to the standard ImageJ method. Furthermore, our regional migration analysis provided accurate and quantitative means to analyse the migration pattern seen in the phantom data and our experimental results, giving us confidence that it can be a robust tool for analysing cell migration patterns.

Keywords

Glioblastoma, Cell migration, Finite element analysis, Spheroid assay

Declarations

Funding

This work is supported by the Ministry of Business, Innovation and Employment of New Zealand Catalyst Grant (PROP-55749-INTCS-UOA), The Neurological Foundation of New Zealand Project Grant, Douglas Charitable Trust, and the Hugh Green Foundation. We would also like to thank the tissue donors for their generous gift of brain tissue for research.

Conflicts of Interest: None

Availability of data, material and code: Not applicable

Authors' contributions: CV conducted the study, performed analysis, wrote the first draft. AW advised numerical analysis, edited the first draft. MD provided the original idea, advised the biological experiment, reviewd the manuscript. TP provided the original idea, designed and supervised the experiment, provided funding, edited the manuscript. VS provided the original idea for the numerical analysis, designed and supervised the analysis, edited the manuscript, provided funding.

Ethics approval : All experiments were conducted with ethical approval by the University of Auckland Human Participants Ethics and the Northern Regional Ethics Committee. The primary cell line used in the experiments were obtained with consent from patients undergoing tumour resection surgery at Auckland City Hospital.

Introduction

Cell migration is an important process regulating physiological (e.g.: capillary formation) and pathological (e.g.: tumour spread) processes. A majority of *in vitro* migration studies use two-dimensional (2D) monolayer cell cultures assays. Wound healing (scraping) and transwell migration (Boyden chamber) assays are some of the more common methods used to study *in vitro* cell migration [1, 2]. More recently, the spheroid assay has emerged in the field of migration studies. This assay combines both two-2D and three-dimensional (3D) technologies to better represent the tissue morphology and cell-cell contacts, without the introduction of cell-free regions [1].

Recent advancements of 3D cultures and experiments have allowed researchers to better mimic *in vivo* conditions such as tissue microstructures and cellular status, both of which can impact proliferation and migration [1, 3]. The formation of spheroids are typically used to investigate tumour growth and viability, and to test anticancer agents [4–6]. Additionally, recent studies show that the spheroids structure provides a better representation of the physiological migration of the cells from a tissue-like structure, which is particularly beneficial in studying tumour cell migration, as solid tumours generally grow as a solid mass [7]. The spheroid assay begins with the attachment of the spheres on the extracellular matrix (ECM)-coated cell culture plate surfaces. Following attachment, cellular migration from the sphere can be influenced by various factors, such as serum [8, 9], chemotactic agents [10, 11], and migration inhibitors [12, 13]. As a result, the cell movement can be measured microscopically and measured at different time-points. This assay can be applied to cell types that can form spheroids, such as neural stem cells [14, 15], certain embryonic stem cells [16, 17], induced pluripotent stem cells (iPSC) and their organoids [18–21], and certain solid tumour cells [7, 22]. The migration of cells is

quantified through measuring the area covered by the cells leaving the sphere [23] or by measuring the normalised radial migratory distance of the cells from the sphere relative to the original diameter of the sphere [24].

Although the above methods are effective at assessing the overall migration of the cells radiating from a sphere, they fall short on providing a quantifiable regional migration analysis in which there are elements of directional migration. Regional migration analysis could prove advantageous as it provides greater insights into migration patterns, more robustly assesses drug treatments on cell migration in a chemotactic fashion, and provides more avenues of experimentation in 2D and 3D models.

One way of analysing regional migration is to create a computational model of the collective cell migration shape and measure the shape changes over time. In computational image analysis, shape changes can be quantified by measuring the amount of deformation between original undeformed and deformed states [25], which is often described as strain. This has advantages over other methods that measure quantitative shape features, such as area and length, because the strain-based method allows more detailed and region-specific analysis in the cell migration patterns.

One method that allows such analysis is Finite Element (FE) models, which have been used extensively in various bioengineering related problems such as joint biomechanics [26, 27], tissue deformation [28] and injury prediction [25]. FE analysis has also been used on a micro-scale such as the work by Saeed and Weihs who simulated a 3D FE cell model and investigated the cell's morphology changes as it underwent uniformly applied compressions [29]. In our previous study, we have used FE analysis to investigate the deformation of cells [30] and cell-seeded 3D hydrogels and characterised the inhomogeneities in strain distribution [31]. Some also used the FE method in analysing cell migration, particularly during wound healing. Most

notably, Zhao and colleagues developed an FE cell migration model that described individual and collective cell movement, as well as the change in cell morphology. The model was consequently used to examine the directionality and persistence of cell migration during re-epithelialisation [32]. However, there are no FE models developed to describe regional cellular migration from spheroid structures, including tumourspheres. Furthermore, many of these studies deployed FE analysis tailored to their own specific purposes, which limits the applicability of those methods to other problems.

In this study, we live-imaged the migration 3D GBM tumoursphere cells and used an FE-based cell migration shape model to analyse various modes of migration readings. This method provides a robust method of regional migrational analysis, allowing researchers the ability to quantitatively assess migration patterns in non-uniform 2D and 3D migration models.

Methods

Ethical approval

All experiments were conducted with ethical approval by the University of Auckland Human Participants Ethics and the Northern Regional Ethics Committee. The primary cell line used in the experiments were obtained with consent from patients undergoing tumour resection surgery at Auckland City Hospital.

Cell Culture

The tumour-initiating cells (TICs) derived from the tissue sample were cultured in T75 flasks containing 10 mL growth factor (GF) stem cell media (DMEM/F12 (Gibco), 1% Penicillin-Streptomycin (Gibco), 1% Glutamax (Invitrogen), 2% B-27 without vitamin A (Invitrogen)) which was supplemented with 2 µg Heparin (Sigma), 50 ng/mL EGF (Invitrogen) and 50

ng/mL FGF (Invitrogen). They were incubated at 37 °C with 95% air, 5% CO_2. Media changes were performed every 2-3 days.

GBM spheroid formation

TICs were harvested for passaging and experimentation by first dissociating the cultures into single-cell suspensions using Accutase® (Invitrogen). In order to generate tumourspheres, TICs were plated at 5000 cells/well in a U-shaped sphere-forming 96-well plate (Thermo Fisher Scientific). Once plated, the cells were incubated at 37 °C with 95% air, 5% CO2 and incubated for 72 hours to ensure proper cell adhesion and sphere formation prior to any experiments.

After incubation, TIC spheres required extraction from the U-shaped plates - The spheres were extracted from the well along with 50 µL of the media in the well into either a Matrigel-coated 12-well plate (for live imaging; 1-2 spheres per well). The plated spheres were then incubated at 37 °C with 95% air, 5% CO_2 for approximately 2-3 hours to ensure successful sphere adherence to the Matrigel®-coated plate. Following adherence, new stem cell media was added into each well – the total volume per well in a 12-well plate should be 1 mL.

Live-imaging of tumoursphere cell migration

After the tumourspheres were plated, they were transferred to the temperature, and CO_2-controlled Live Cell Microscope Incubator (Zeiss XL-3 stage incubation chamber) fitted with the Axiovert 200M motorised inverted microscope and AxioCam MRm digital camera (Zeiss). The temperature and CO_2 levels were maintained at 37 °C and 5% respectively within the chamber and adequately humidified to prevent excessive evaporation. The microscope magnification was maintained at 10X with 0.25 bright-field images using A-plan every 20 minutes using the AxioVision program associated with the imaging suite (Zeiss) over the time course of 48 hours. Colour and exposure settings were set at Black and White settings to ensure a clear distinction and focus of migrating cells.

Migration analysis of tumoursphere cells

After the images were captured, they were first imported into ImageJ. ImageJ migration area analysis began by highlighting the the 'Find Edges' operation and thresholding. The area was subsequently measured using the magic wand tool and finding the net difference between the migration area and sphere area. The boundaries of these areas were stacked together and stored as 3D clouds of data points for mesh morphing described below.

First, we generated a reference mesh in the shape of a donut that approximates migration patterns of the core and the boundary of the cell aggregates separately. We used high order cubic Hermite basis function with hexahedral elements to capture the complex shape changes over time[33]. This was then morphed to match the migrating pattern at various time points [Figure 1].

We used our mesh morphing algorithm, which orthogonally projects a cloud of data points to the mesh surfaces. The reference mesh was then deformed to match the shape of the cloud of data points using the least square fit algorithm (Equation 1)[33].

$$F(u_n) = \sum_{d=1}^{n} \|u(\xi_{1d}, \xi_{2d}) - z_d\|^2 + F_s(u_n) \qquad \textbf{(1)}$$

Where z_d are the coordinates of data points and ξ_{1d}, ξ_{2d} are the results of the orthogonal projection of data points to the surface of the mesh. F_s is the penalty function which ensures the geometric smoothness of the mesh. The expression of the penalty function is given in Equation 2:

$$F_s(u_n) = \int_0^1 \int_0^1 \left\{ \propto_1 \left\| \frac{\partial u}{\partial \xi} \right\|^2 + \propto_2 \left\| \frac{\partial u}{\partial \xi} \right\|^2 + \propto_3 \left\| \frac{\partial u}{\partial \xi} \right\|^2 + \propto_4 \left\| \frac{\partial u}{\partial \xi} \right\|^2 + \propto_5 \left\| \frac{\partial u}{\partial \xi} \right\|^2 \right\} d\xi_1 d\xi_2 \qquad \textbf{(2)}$$

Where $\propto_i$ (i = 1…5) are penalty parameters. Each of these terms has a distinct effect on the final shape of the fitted mesh; $\propto_1$ and $\propto_2$ terms control arc-length, while $\propto_3$ and $\propto_4$ control the arc-curvature in the ξ_1 and ξ_2 directions, respectively.

The resultant meshes were generated at different time points and imported for FE analysis [Figure 1]. From this, the changes in the migrating areas can be obtained by solving the governing equation that describes the deformation of an object at different time points. This was achieved by solving the static Cauchy equation (Equation 3).

$$\frac{\partial \sigma_{ij}}{\partial x_j} + \rho \cdot b_i = 0 : i,j = 1..3 \qquad \textbf{(3)}$$

Where σ_{ij} are the Cauchy stress tensor components, x_j are spatial coordinates. b_j are body force components, and ρ is the soft tissue density; both variables were neglected in this case.

To quantify the migration rates, displacement boundary conditions were used as the migration pattern of the cells was already known from the images at different time points. This prescribed the nodal positions at each time point and our finite element solver computed for the remaining degrees of freedom. Then the change in the migration pattern was analysed using strain, which was calculated in the form of Lagrangian strain using the theory of finite deformation elasticity as in our previous study [30, 34]. The strain between original and deformed (i.e. time lapsed) meshes was computed using the deformation gradient tensor between the two, which is quantified by measuring the change in length of material segments [30, 34]. Given a material vector in the undeformed state (d**X**) which is mapped to the deformed state (d**x**), the gradient deformation tensor (F) is defined as the following (Equation 4)

$$\mathbf{F} = \frac{d\boldsymbol{x}}{d\boldsymbol{X}} \qquad \textbf{(4)}$$

Strain in a deformed mesh is determined by measuring segment length changes, which is done by computing the square length (ds^2) for the deformed segment d**x** giving (Equation 5)

$$ds^2 = dx^i x^i = d\boldsymbol{x}^T d\boldsymbol{x} = (\boldsymbol{F}d\boldsymbol{X})^T \boldsymbol{F}d\boldsymbol{X} = d\boldsymbol{X}^T \boldsymbol{F}^T \boldsymbol{F}d\boldsymbol{X} = d\boldsymbol{X}^T \boldsymbol{C}d\boldsymbol{X} \qquad \textbf{(5)}$$

From this, we calculate the Cauchy-Green deformation tensor (Equation 6):

195 $$\boldsymbol{C = F^T F} \qquad \textbf{(6)}$$

196 Finally, using the deformation, we derive the Lagrangian finite strain tensor (Equation 7):

197 $$\boldsymbol{E = \frac{(C-I)}{2}} \qquad \textbf{(7)}$$

198 The cell deformation and internal strain patterns in tumoursphere at each time point were
199 described with the final Lagrangian strain tensor. As for the material properties, since our main
200 focus is the analysis of the overall migration area, we ignored any nonlinear viscoelastic
201 behaviour that might occur in the internal region of the cell aggregates. Therefore, the cell
202 aggregates were modelled with a hyperelastic Mooney Rivelin material with a homogenous
203 property. The parameter C_1 and C_2 values were obtained from the experimental study of the
204 tumor tissue [35]. We used the maximum principal strain from the final deformed mesh to
205 describe the migration rate. We used our in-house FE software called CMISS, that is freely
206 available for academic use for migration analysis (www.opencmiss. org).

207 ## Statistical analysis

208 Graphing and statistical analysis were performed using GraphPad Prism 8 (GraphPad Software
209 Inc.). Correlation analysis was achieved in GraphPad Prism 8. Graphs with error bars were
210 displayed as means ± standard error of measurement (SEM), and statistical significance was
211 set at $p < 0.05$. Two-way ANOVA with Dunnet's post-test group comparison was completed.

212

Results

ImageJ vs FE-based area analysis

The rate and the overall area of migration are key metrics analysed in cellular migration experiments. When involving the migration from spheroid structures, such as tumourspheres, ImageJ area calculation has often been employed to measure these parameters. The aim of this section was to validate the FE analysis capability to achieve the level of accuracy offered by these standard methods of analysis. In order to validate our analysis, the tumoursphere migration rate and overall area were assessed using both the established ImageJ protocols and our FE analysis protocol.

Figure 2 shows ImageJ and FE area analysis of two migrating tumoursphere repeats. The correlation analysis between ImageJ and FE areas showed very high Pearson correlation, with an R^2 of 0.9917 in tumoursphere repeat 1, and R^2 of 0.9835 in tumoursphere repeat 2 (Figure 2 A-2 and B-2 respectively). This confirms the accuracy of area analysis done by our FE based method.

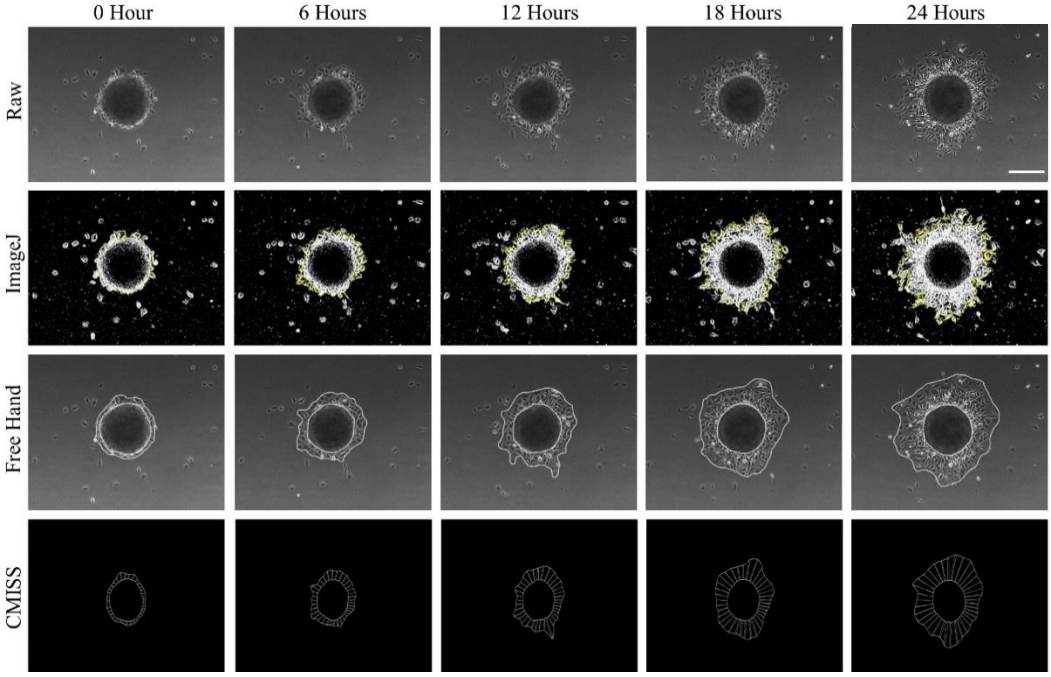

Figure 1. Processing of a representative tumoursphere sample for ImageJ and FE model images. Area measurement using ImageJ was achieved by identifying the boundaries using the magic wand tool on thresholded images. FE area analysis required a Free Hand boundary region before it was imported into our FE analysis software as a mesh and the area was measured. White scale bar 250 µm. The 2D view of the 3D FE model is

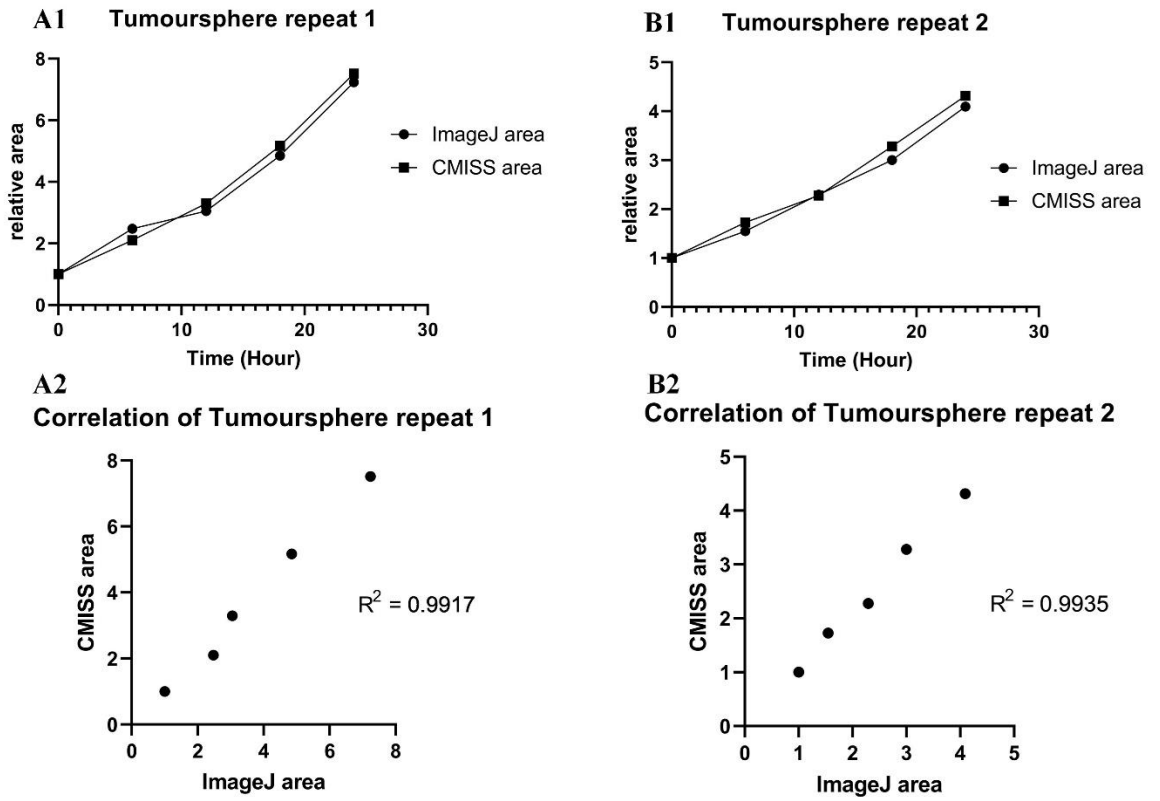

Figure 2. Changes in area measured in ImageJ and FE analysis correlated very highly with each other. Overall area was measured using ImageJ and our FE based method over 24 hours in 6 hour increments on two migrating tumoursphere repeats (A1 and B1). The areas were correlated using the William Pearson Correlation analysis in Graphpad Prism 8 and the R^2 was measured (A2 and B2).

FE-Regional Migration Rate Analysis

Phantom data with an evident preferential migration was firstly used to show the capabilities of our FE based method to quantify the directionality of migration. The analysis method was further applied to a real tumoursphere sample with a more nuanced migration to evaluate its effectiveness in a real-life example.

Figure 3 illustrates the preferential rightward migration of the phantom data, which is visualised by the red data points in Figure 3-A2. The data points were segmented into 60˚ quantifiable regions, with significantly greater migration distance detected in the 120˚ segment throughout the four time points ($p<0.0001$) when compared to all other segments (Figure 3-B). The ability to delineate and measure regional migration rates are illustrated in Figure 3-C. For example, the rate at which the 120˚ segment migrated was significantly higher during the first time-point ($p<0.0001$), which faithfully represented the phantom data is analysed (Figure 3-

239 A2). Overall, the phantom data results allowed for optimisation and validation of the FE-based
240 approach to quantify regional migration.

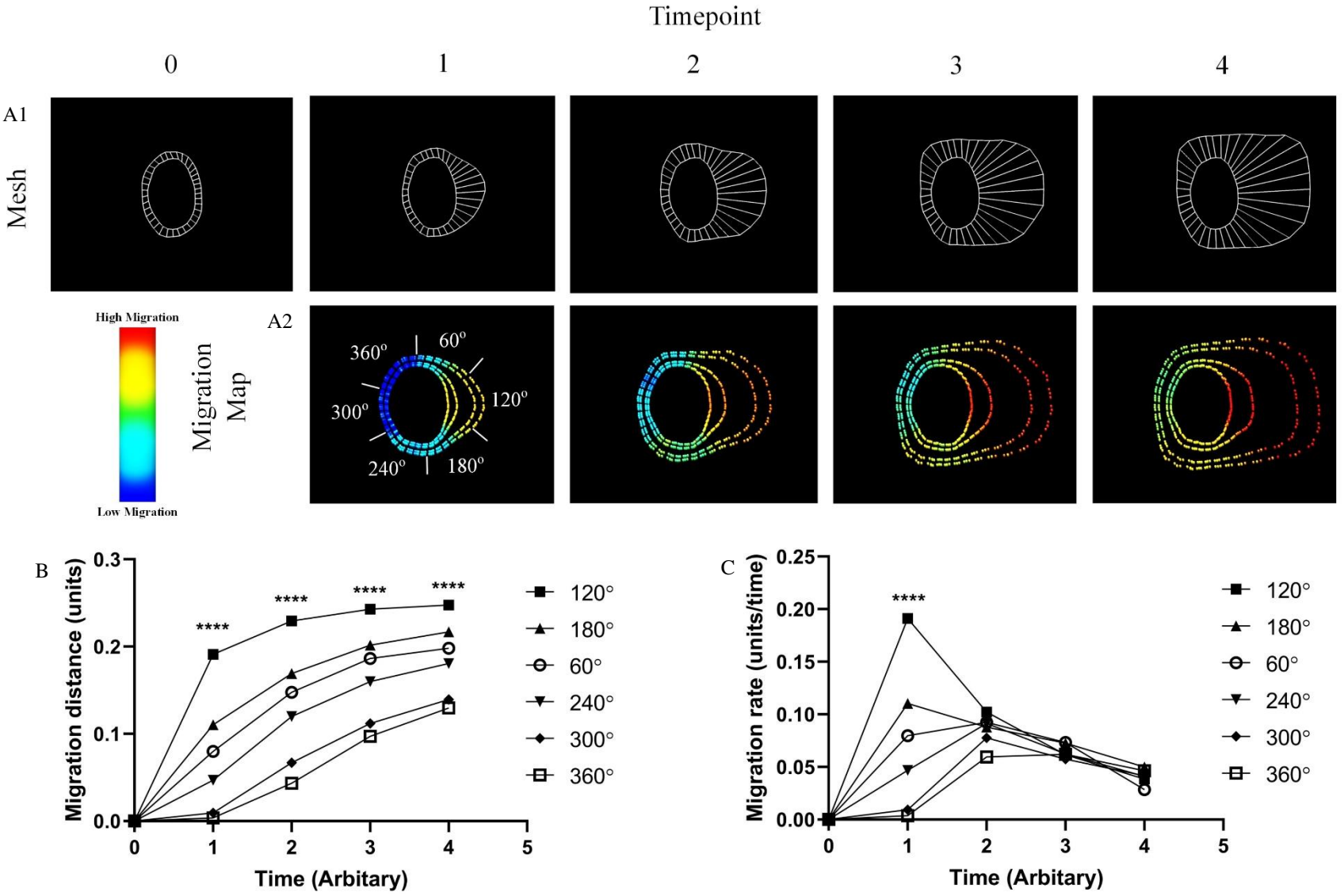

Figure 3. Our FE-based approach accurately quantified regional migration of the phantom data. The phantom data mesh (A1) was utilised in our FE models to quantify the migration rate over time which was visualised in the migration map (Red indicates high migration rate while blue indicates minimal migration rate; A2). Data points in the migration map were segmented in 60˚ increments and averaged, before they were plotted and compared against each other (B). Every segment at each timepoint were compared against the 120˚ segment and statistical significance was assessed via Two-way ANOVA test with Dunnett's post-test; ****p<0.0001 all segments versus 120˚ segment (B). Migration rate was calculated by finding the difference in migration distances between the current timepoint and the previous timepoint, and the difference was divided by the time that has passed between the two timepoints (C).

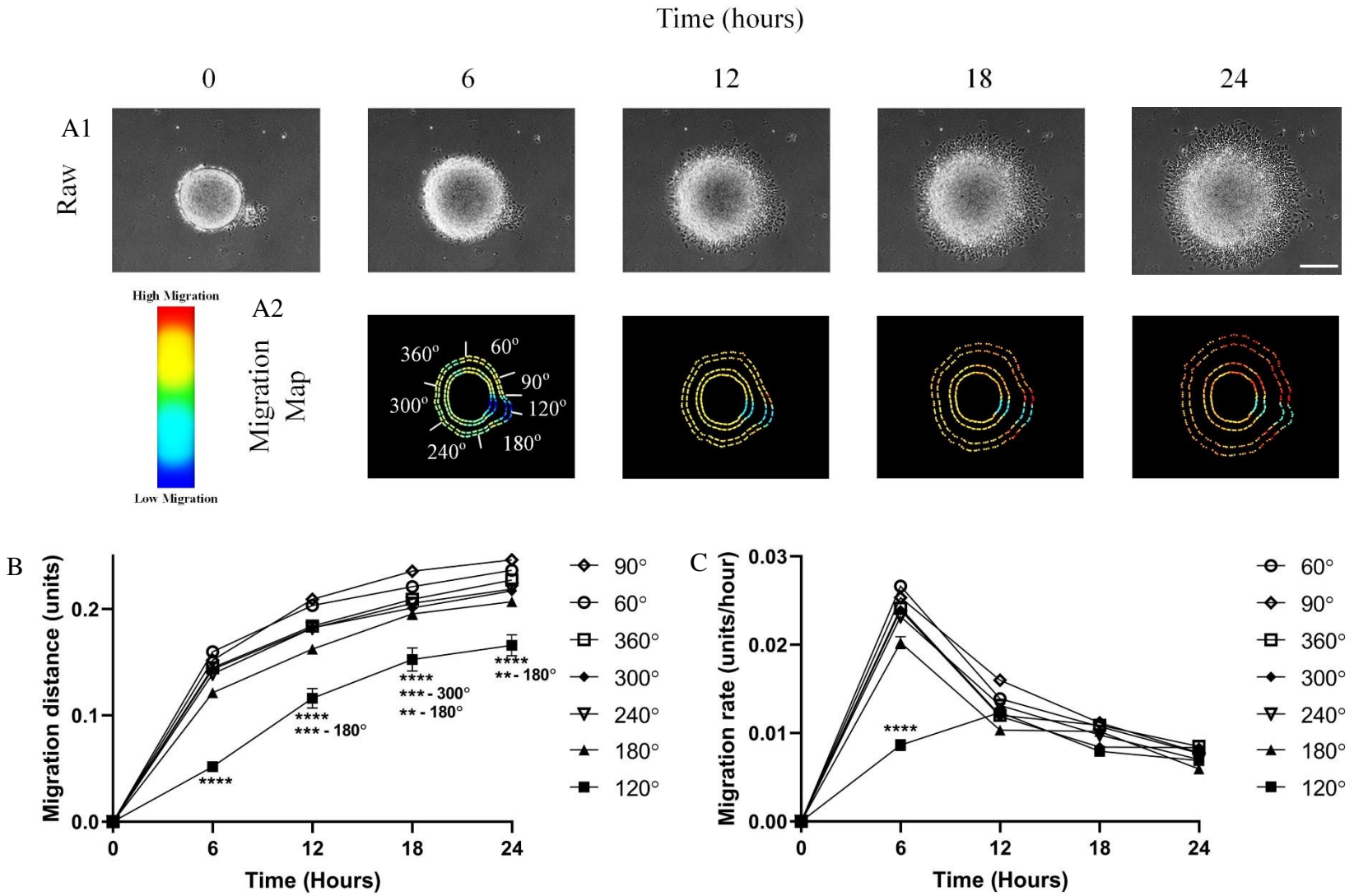

Figure 4. FE-based analysis was capable of detecting and quantifying the nuanced migration. The images of the the migrating tumoursphere were taken every 6 hours for 24 hours (A1) and were analysed by our FE models to produce the migration maps (Red indicates high migration rate while blue indicates minimal migration rate; A2). The data points from the migration maps were plotted and graphed in segments to assess the regional migration of the tumoursphere. Every segment at each timepoint were compared against the 120˚ segment and statistical significance was assessed via Two-way ANOVA test with Dunnett's post-test; **p<0.005, ***p<0.0005, ****p<0.0001 all segments versus 120˚ segment, and different *p from different segment comparisons are outlined in the graph (B). Migration rate was calculated by finding the difference in migration distances between the current timepoint and the previous timepoint, and the difference was divided by the time that has passed between the two timepoints (C). White scale bar represents 250 µm.

In Figure 4, the tumoursphere exhibited an unexpected protrusion of cells on the right side, which did not migrate as much as the rest of the tumoursphere throughout the first 24 hours. Quantification of the tumoursphere migration showed a relatively low migration rate at the 120˚ segment (Figure 4-B), which corresponded to the lack of migration in the area of cellular protrusion. Moreover, the migration distance of the 120˚ segment was significantly lower than all other segments throughout the 24 hours (Figure 4-B), while the migration rate was significantly lower than all other segments in the first 6 hours (Figure 4-C). However, only the 120˚ segment showed a steady increase in migration rate over the first 12 hours while all other segments decreased over the same period (Figure 4-C). Overall, our FE-based approach was able to detect and quantify the variations in a sphere shape and migrational patterns of cells from live tumourspheres.

Discussion

In this study, we have developed a FE-based method that can measure the area changes, as well as the directionalities of the change in a tumoursphere model. Our method was highly comparable to the area changes measured by ImageJ - a standard tool used by many investigators to assess the overall cellular migration. Furthermore, the strength of our FE-based method is in its ability to analyse regional migration in GBM tumourspheres, as the migration rates of the FE tumoursphere model faithfully represented to the migration pattern of phantom data and actual experimental results. This type of regional analysis is not possible using ImageJ.

Our pipeline is able to section the tumoursphere into any desired segments during our analyses. This allows the investigation of migration from different radial regions of the sphere that could detect and quantify non-uniform migratory patterns that could have been missed using conventional overall area change models. Furthermore, the current pipeline involves the segmentation of raw images into boundary lines and the fitting of a mesh onto the boundary lines, therefore broadening the applications for this pipeline. For example, this pipeline can be applied to other migration models such as wound-healing/scratch assays [36–40], as the boundary of migration can be defined, and a mesh can be constructed and overlayed. For instance, Zepecki observed that Lck-inhibition in tumoursphere cells resulted in reduced cellular migration when compared to the controls [41]. Additionally, Zepecki and colleagues analysed the tumour growth in a 3D brain reconstruction of a growing tumour within a mouse's brain using Neurolucida explorer (MBF Biosciences)[41]. Hypothetically, these observations could be analysed using our pipeline to provide a quantifiable measure of migration, both *in vitro* and *in vivo*. Moreover, all tumoursphere migration analyses from a recent literature survey revealed that only the overall migration area was used to quantify tumoursphere migration propensity [7, 23, 24]. Our pipeline can include additional analysis modes, such as overall

migration rate and more importantly, regional migration rate. As a result, this can provide a deep, and potentially, novel insight into migration patterns of cells, especially in response to migration modifying agents, such as extracellular matrix and cell surface modifications [42–45], chemotactic agents [46–49] and small molecular agents [50–53].

Moreover, our pipeline uses 3D FE models. In the current study, only 2D images were available hence they were stacked up to generate 3D cloud of data points, which were then used to morph our 3D model. But if 3D images exist (e.g. from confocal microscopy images), our models can capture the migration pattern changes in 3D, making it an ideal tool for investigating the actual *in vivo* migration pattern from patients clinical images such as MRI.

Although the study shows promise in analysing regional migration in spheroid models, there are areas where improvements are required. First, the assumption of our analysis is that the boundary motion is the major factor that influence the movement of the entire cellular aggregate. Hence it will not be able to describe the movements of the cell in the centre region of the aggregates. This will require a non-linear viscoelastic material descriptions, yet parameters for such complex material descriptions for tumour cells have not been studied or estimated, making it not possible to incorporate in the modelling framework. Moreover, our main aim is to characterise the overall migration pattern of the cell aggregates and our experimental data consistently showed that it is dominated by the movement of boundary cells. Hence our assumption was appropriate for the study purpose. Secondly, the current pipeline requires manual processing of the images, which hinders the efficiency and scalability of the method. Moreover, FE-based methods are not widely used to analyse cellular/molecular biological processes; hence it may be difficult for users without prior experience in FE analysis to apply our method to their studies. Finally, the multiple steps required to execute the entire

pipeline has not been integrated into a single streamlined process, hence making it more complicated for users without experience in scripting languages. Some of these issues are currently being addressed by uniting many of the pipeline's steps under one programming language such as Python, since OpenCV and FE modules in Python are capable of accomplishing many if not all of the steps in the current pipeline. As a result, a program made under one programming language will be more accessible to the broader audience and will be more integrated than the existing pipeline. We aim to report this progress in our next publication.

In conclusion, we have developed a novel customisable FE-based analysis algorithm that can be to detect regional changes in cellular migration and accurately quantify various migratory matrices. This can pave the way for more automated analyses of brain tumour migration patterns both in *in vitro* experiments and *in vivo* medical images.

References

1. Kramer, N., Walzl, A., Unger, C., Rosner, M., Krupitza, G., Hengstschläger, M., & Dolznig, H. (2013, January 1). In vitro cell migration and invasion assays. *Mutation Research - Reviews in Mutation Research*. Elsevier. https://doi.org/10.1016/j.mrrev.2012.08.001

2. Riahi, R., Yang, Y., Zhang, D. D., & Wong, P. K. (2012). Advances in Wound-Healing Assays for Probing Collective Cell Migration. *Journal of Laboratory Automation*, *17*(1), 59–65. https://doi.org/10.1177/2211068211426550

3. Duval, K., Grover, H., Han, L.-H., Mou, Y., Pegoraro, A. F., Fredberg, J., & Chen, Z. (2017). Modeling Physiological Events in 2D vs. 3D Cell Culture. *Physiology*, *32*(4), 266–277. https://doi.org/10.1152/physiol.00036.2016

4. Christman, J. K. (2002). 5-Azacytidine and 5-aza-2′-deoxycytidine as inhibitors of DNA methylation: mechanistic studies and their implications for cancer therapy. *Oncogene*, *21*(35), 5483–5495. https://doi.org/10.1038/sj.onc.1205699

5. Lee, C. H., Yu, C. C., Wang, B. Y., & Chang, W. W. (2016). Tumorsphere as an effective in vitro platform for screening anticancer stem cell drugs. *Oncotarget*, *7*(2), 1215–1226. https://doi.org/10.18632/oncotarget.6261

6. Nonaka, M., Yawata, T., Takemura, M., Higashi, Y., Nakai, E., Shimizu, K., & Ueba, T. (2014). Elevated cell invasion in a tumor sphere culture of RSV-M mouse glioma cells. *Neurologia Medico-Chirurgica*, *55*(1), 60–70. https://doi.org/10.2176/nmc.oa.2014-0067

7. Gudbergsson, J. M., Kostrikov, S., Johnsen, K. B., Fliedner, F. P., Stolberg, C. B., Humle, N., … Duroux, M. (2019). A tumorsphere model of glioblastoma multiforme with intratumoral heterogeneity for quantitative analysis of cellular migration and drug response. *Experimental Cell Research*, *379*(1), 73–82. https://doi.org/10.1016/J.YEXCR.2019.03.031

8. Hong, X., Chedid, K., & Kalkanis, S. N. (2012). Glioblastoma cell line-derived spheres in serum-containing medium versus serum-free medium: A comparison of cancer stem cell properties. *International Journal of Oncology*, *41*(5), 1693–1700. https://doi.org/10.3892/ijo.2012.1592

9. Joseph, J. V., Roosmalen, I. A. M. van, Busschers, E., Tomar, T., Conroy, S., Eggens-Meijer, E., … Kruyt, F. A. E. (2015). Serum-Induced Differentiation of Glioblastoma Neurospheres Leads to Enhanced Migration/Invasion Capacity That Is Associated with Increased MMP9. *PLOS ONE*, *10*(12), e0145393. https://doi.org/10.1371/journal.pone.0145393

10. Dziembowska, M., Tham, T. N., Lau, P., Vitry, S., Lazarini, F., & Dubois-Dalcq, M. (2005). A role for CXCR4 signaling in survival and migration of neural and oligodendrocyte precursors. *Glia*, *50*(3), 258–269. https://doi.org/10.1002/glia.20170

11. Filippo, T. R. M., Galindo, L. T., Barnabe, G. F., Ariza, C. B., Mello, L. E., Juliano, M. A., … Porcionatto, M. A. (2013). CXCL12 N-terminal end is sufficient to induce chemotaxis and proliferation of neural stem/progenitor cells. *Stem Cell Research*, *11*(2), 913–925. https://doi.org/10.1016/j.scr.2013.06.003

12. Fehlauer, F., Muench, M., Rades, D., Stalpers, L. J. A., Leenstra, S., Van Der Valk, P., … Sminia, P. (2005). Effects of irradiation and cisplatin on human glioma spheroids: Inhibition of cell proliferation and cell migration. *Journal of Cancer Research and Clinical Oncology*, *131*(11), 723–732. https://doi.org/10.1007/s00432-005-0014-3

13. Peiris-Pagès, M., Bonuccelli, G., Sotgia, F., & Lisanti, M. P. (2018). Mitochondrial fission as a driver of stemness in tumor cells: mDIVI1 inhibits mitochondrial function, cell migration and cancer stem cell (CSC) signalling. *Oncotarget*, *9*(17), 13254–13275. https://doi.org/10.18632/oncotarget.24285

14. Uchida, N., Buck, D. W., He, D., Reitsma, M. J., Masek, M., Phan, T. V., … Weissman, I. L. (2000). Direct isolation of human central nervous system stem cells. *Proceedings of the National Academy of Sciences of the United States of America*, *97*(26), 14720–14725. https://doi.org/10.1073/pnas.97.26.14720

15. Reynolds, B. A., & Weiss, S. (1992). Generation of neurons and astrocytes from isolated cells of the adult mammalian central nervous system. *Science*, *255*(5052), 1707–1710. https://doi.org/10.1126/science.1553558

16. Subramanian, K., Owens, D. J., Raju, R., Firpo, M., O'Brien, T. D., Verfaillie, C. M., & Hu, W. S. (2014). Spheroid culture for enhanced differentiation of human

embryonic stem cells to hepatocyte-like cells. *Stem Cells and Development*, *23*(2), 124–131. https://doi.org/10.1089/scd.2013.0097

17. Faulkner-Jones, A., Greenhough, S., A King, J., Gardner, J., Courtney, A., & Shu, W. (2013). Development of a valve-based cell printer for the formation of human embryonic stem cell spheroid aggregates. *Biofabrication*, *5*(1), 015013. https://doi.org/10.1088/1758-5082/5/1/015013

18. Beauchamp, P., Moritz, W., Kelm, J. M., Ullrich, N. D., Agarkova, I., Anson, B. D., … Zuppinger, C. (2015). Development and Characterization of a Scaffold-Free 3D Spheroid Model of Induced Pluripotent Stem Cell-Derived Human Cardiomyocytes. *Tissue Engineering - Part C: Methods*, *21*(8), 852–861. https://doi.org/10.1089/ten.tec.2014.0376

19. Freedman, B. S., Brooks, C. R., Lam, A. Q., Fu, H., Morizane, R., Agrawal, V., … Bonventre, J. V. (2015). Modelling kidney disease with CRISPR-mutant kidney organoids derived from human pluripotent epiblast spheroids. *Nature Communications*, *6*(1), 8715. https://doi.org/10.1038/ncomms9715

20. Gotoh, S., Ito, I., Nagasaki, T., Yamamoto, Y., Konishi, S., Korogi, Y., … Mishima, M. (2014). Generation of alveolar epithelial spheroids via isolated progenitor cells from human pluripotent stem cells. *Stem Cell Reports*, *3*(3), 394–403. https://doi.org/10.1016/j.stemcr.2014.07.005

21. Mustata, R. C., Vasile, G., Fernandez-Vallone, V., Strollo, S., Lefort, A., Libert, F., … Garcia, M. I. (2013). Identification of Lgr5-Independent Spheroid-Generating Progenitors of the Mouse Fetal Intestinal Epithelium. *Cell Reports*, *5*(2), 421–432. https://doi.org/10.1016/j.celrep.2013.09.005

22. Glinka, Y., Mohammed, N., Subramaniam, V., Jothy, S., & Prud'homme, G. J. (2012).

Neuropilin-1 is expressed by breast cancer stem-like cells and is linked to NF-κB activation and tumor sphere formation. *Biochemical and Biophysical Research Communications*, *425*(4), 775–780. https://doi.org/10.1016/j.bbrc.2012.07.151

23. Vinci, M., Box, C., Zimmermann, M., & Eccles, S. A. (2013). Tumor Spheroid-Based Migration Assays for Evaluation of Therapeutic Agents (pp. 253–266). Humana Press, Totowa, NJ. https://doi.org/10.1007/978-1-62703-311-4_16

24. Deryugina, E. I., & Bourdon, M. A. (1996). Tenascin mediates human glioma cell migration and modulates cell migration on fibronectin. *Journal of Cell Science*, *109*(3).

25. Shim, V. B., Holdsworth, S., Champagne, A. A., Coverdale, N. S., Cook, D. J., Lee, T.-R., … Fernandez, J. W. (2020). Rapid Prediction of Brain Injury Pattern in mTBI by Combining FE Analysis With a Machine-Learning Based Approach. *IEEE Access*, *8*, 179457–179465. https://doi.org/10.1109/access.2020.3026350

26. Chen, T. L. W., Wong, D. W. C., Wang, Y., Lin, J., & Zhang, M. (2019). Foot arch deformation and plantar fascia loading during running with rearfoot strike and forefoot strike: A dynamic finite element analysis. *Journal of Biomechanics*, *83*, 260–272. https://doi.org/10.1016/j.jbiomech.2018.12.007

27. Peña, E., Calvo, B., Martínez, M. A., & Doblaré, M. (2006). A three-dimensional finite element analysis of the combined behavior of ligaments and menisci in the healthy human knee joint. *Journal of Biomechanics*, *39*(9), 1686–1701. https://doi.org/10.1016/j.jbiomech.2005.04.030

28. Nash, M. P., & Hunter, P. J. (2000). Computational mechanics of the heart. From tissue structure to ventricular function. *Journal of Elasticity*. Springer. https://doi.org/10.1023/A:1011084330767

29. Saeed, M., & Weihs, D. (2020). Finite element analysis reveals an important role for cell morphology in response to mechanical compression. *Biomechanics and Modeling in Mechanobiology*, *19*(3), 1155–1164. https://doi.org/10.1007/s10237-019-01276-5

30. Kim, J. J., Musson, D. S., Matthews, B. G., Cornish, J., Anderson, I. A., & Shim, V. B. (2016). Applying Physiologically Relevant Strains to Tenocytes in an in Vitro Cell Device Induces in Vivo Like Behaviors. *Journal of Biomechanical Engineering*, *138*(12). https://doi.org/10.1115/1.4034031

31. Leung, S., McGlashan, S. R., Musson, D. S. P., Cornish, J., Anderson, I. A., & Shim, V. B. K. (2018). Investigations of Strain Fields in 3D Hydrogels Under Dynamic Confined Loading. *Journal of Medical and Biological Engineering*, *38*(3), 514–522. https://doi.org/10.1007/s40846-017-0319-0

32. Zhao, J., Cao, Y., Di Pietro, L. A., & Liang, J. (2017). Dynamic cellular finite-element method for modelling large-scale cell migration and proliferation under the control of mechanical and biochemical cues: A study of re-epithelialization. *Journal of the Royal Society Interface*, *14*(129), 20160959. https://doi.org/10.6084/m9.figshare.c.3726151

33. Fernandez, J. W., Mithraratne, P., Thrupp, S. F., Tawhai, M. H., & Hunter, P. J. (2004). Anatomically based geometric modelling of the musculo-skeletal system and other organs. *Biomechanics and Modeling in Mechanobiology*, *2*(3), 139–155. https://doi.org/10.1007/s10237-003-0036-1

34. Leung, S., Kim, J., Musson, M., McGlashan, S., Cornish, J., Anderson, I., & Shim, V. (2021). A novel in vitro and in silico system for analysing complex mechanobiological behaviour of chondrocytes in 3D hydrogel construct. *ASM Journal of Biomechanical Engineering*.

35. Dastjerdi, M. M., Fallah, A., & Rashidi, S. (2019). An Iterative Method for Estimating

Nonlinear Elastic Constants of Tumor in Soft Tissue from Approximate Displacement Measurements. *Journal of Healthcare Engineering*, *2019*. https://doi.org/10.1155/2019/2374645

36. Fronza, M., Heinzmann, B., Hamburger, M., Laufer, S., & Merfort, I. (2009). Determination of the wound healing effect of Calendula extracts using the scratch assay with 3T3 fibroblasts. *Journal of Ethnopharmacology*, *126*(3), 463–467. https://doi.org/10.1016/j.jep.2009.09.014

37. Yang, M., Li, Y., Chilukuri, K., Brady, O. A., Boulos, M. I., Kappes, J. C., & Galileo, D. S. (2011). L1 stimulation of human glioma cell motility correlates with FAK activation. *Journal of Neuro-Oncology*, *105*(1), 27–44. https://doi.org/10.1007/s11060-011-0557-x

38. Zubair, M., Ekholm, A., Nybom, H., Renvert, S., Widen, C., & Rumpunen, K. (2012). Effects of Plantago major L. leaf extracts on oral epithelial cells in a scratch assay. *Journal of Ethnopharmacology*, *141*(3), 825–830. https://doi.org/10.1016/j.jep.2012.03.016

39. Pinto, B. I., Cruz, N. D., Lujan, O. R., Propper, C. R., & Kellar, R. S. (2019). In Vitro Scratch Assay to Demonstrate Effects of Arsenic on Skin Cell Migration. *Journal of visualized experiments : JoVE*, (144). https://doi.org/10.3791/58838

40. Belkacemi, A., Laschke, M. W., Menger, M. D., & Flockerzi, V. (2019). Scratch migration assay and dorsal skinfold chamber for in vitro and in vivo analysis of wound healing. *Journal of Visualized Experiments*, *2019*(151), 59608. https://doi.org/10.3791/59608

41. Zepecki, J. P., Snyder, K. M., Moreno, M. M., Fajardo, E., Fiser, A., Ness, J., … Tapinos, N. (2019). Regulation of human glioma cell migration, tumor growth, and

stemness gene expression using a Lck targeted inhibitor. *Oncogene*, *38*(10), 1734–1750. https://doi.org/10.1038/s41388-018-0546-z

42. Itoh, Y. (2006, October 1). MT1-MMP: A key regulator of cell migration in tissue. *IUBMB Life*. John Wiley & Sons, Ltd. https://doi.org/10.1080/15216540600962818

43. Webb, A. H., Gao, B. T., Goldsmith, Z. K., Irvine, A. S., Saleh, N., Lee, R. P., … Morales-Tirado, V. M. (2017). Inhibition of MMP-2 and MMP-9 decreases cellular migration, and angiogenesis in in vitro models of retinoblastoma. *BMC Cancer*, *17*(1), 434. https://doi.org/10.1186/s12885-017-3418-y

44. Franceschini, I., Vitry, S., Padilla, F., Casanova, P., Tham, T. N., Fukuda, M., … Dubois-Dalcq, M. (2004). Migrating and myelinating potential of neural precursors engineered to overexpress PSA-NCAM. *Molecular and Cellular Neuroscience*, *27*(2), 151–162. https://doi.org/10.1016/j.mcn.2004.05.006

45. Vitry, S., Avellana-Adalid, V., Lachapelle, F., & Baron-Van Evercooren, A. (2001). Migration and multipotentiality of PSA-NCAM+ neural precursors transplanted in the developing brain. *Molecular and Cellular Neuroscience*, *17*(6), 983–1000. https://doi.org/10.1006/mcne.2001.0987

46. Badolato, R., Wang, J. M., Murphy, W. J., Lloyd, A. R., Michiel, D. F., Bausserman, L. L., … Oppenheim, J. J. (1994). Serum amyloid a is a chemoattractant: Induction migration, adhesion, and tissue infiltration of monocytes and polymorphonuclear leukocytes. *Journal of Experimental Medicine*, *180*(1), 203–209. https://doi.org/10.1084/jem.180.1.203

47. Zhao, M., Agius-Fernandez, A., Forrester, J. V, & McCaig, C. D. (1996). Orientation and directed migration of cultured corneal epithelial cells in small electric fields are serum dependent. *Journal of Cell Science*, *109*(6), 1405 LP – 1414. Retrieved from

http://jcs.biologists.org/content/109/6/1405.abstract

48. Li, M., Sun, X., Ma, L., Jin, L., Zhang, W., Xiao, M., & Yu, Q. (2017). SDF-1/CXCR4 axis induces human dental pulp stem cell migration through FAK/PI3K/Akt and GSK3β/β-catenin pathways. *Scientific Reports*, *7*(1), 1–13. https://doi.org/10.1038/srep40161

49. Marquez-Curtis, L. A., & Janowska-Wieczorek, A. (2013). Enhancing the migration ability of mesenchymal stromal cells by targeting the SDF-1/CXCR4 axis. *BioMed Research International*. https://doi.org/10.1155/2013/561098

50. Xia, C., Liang, S., He, Z., Zhu, X., Chen, R., & Chen, J. (2018). Metformin, a first-line drug for type 2 diabetes mellitus, disrupts the MALAT1/miR-142-3p sponge to decrease invasion and migration in cervical cancer cells. *European Journal of Pharmacology*, *830*, 59–67. https://doi.org/10.1016/j.ejphar.2018.04.027

51. Huang, Y., Li, Q., Tian, H., Yao, X., Bakina, O., Zhang, H., … Hu, F. (2020). MEK inhibitor trametinib attenuates neuroinflammation and cognitive deficits following traumatic brain injury in mice. *American journal of translational research*, *12*(10), 6351–6365. Retrieved from http://www.ncbi.nlm.nih.gov/pubmed/33194035

52. Daga, M., Pizzimenti, S., Dianzani, C., Cucci, M. A., Cavalli, R., Grattarola, M., … Barrera, G. (2019). Ailanthone inhibits cell growth and migration of cisplatin resistant bladder cancer cells through down-regulation of Nrf2, YAP, and c-Myc expression. *Phytomedicine*, *56*, 156–164. https://doi.org/10.1016/j.phymed.2018.10.034

53. Sun, X. J., Zhang, P., Li, H. H., Jiang, Z. W., Jiang, C. C., & Liu, H. (2014). Cisplatin combined with metformin inhibits migration and invasion of human nasopharyngeal carcinoma cells by regulating E-cadherin and MMP-9. *Asian Pacific Journal of Cancer Prevention*, *15*(9), 4019–4023. https://doi.org/10.7314/APJCP.2014.15.9.4019

513

514

515

516

Figures

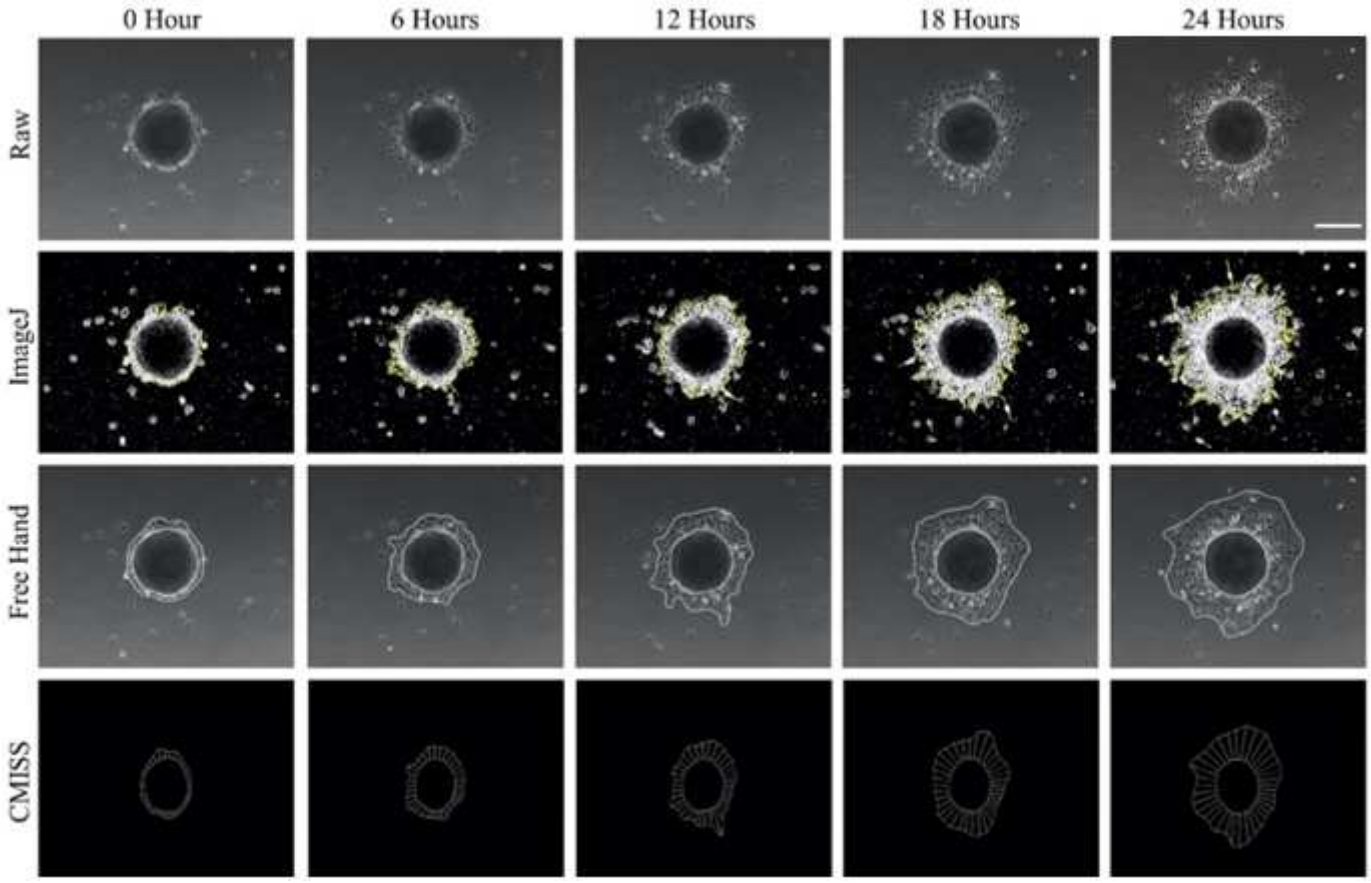

Figure 1

Processing of a representative tumoursphere sample for ImageJ and FE model images. Area measurement using ImageJ was achieved by identifying the boundaries using the magic wand tool on thresholded images. FE area analysis required a Free Hand boundary region before it was imported into our FE analysis software as a mesh and the area was measured. White scale bar 250 μm. The 2D view of the 3D FE model is shown.

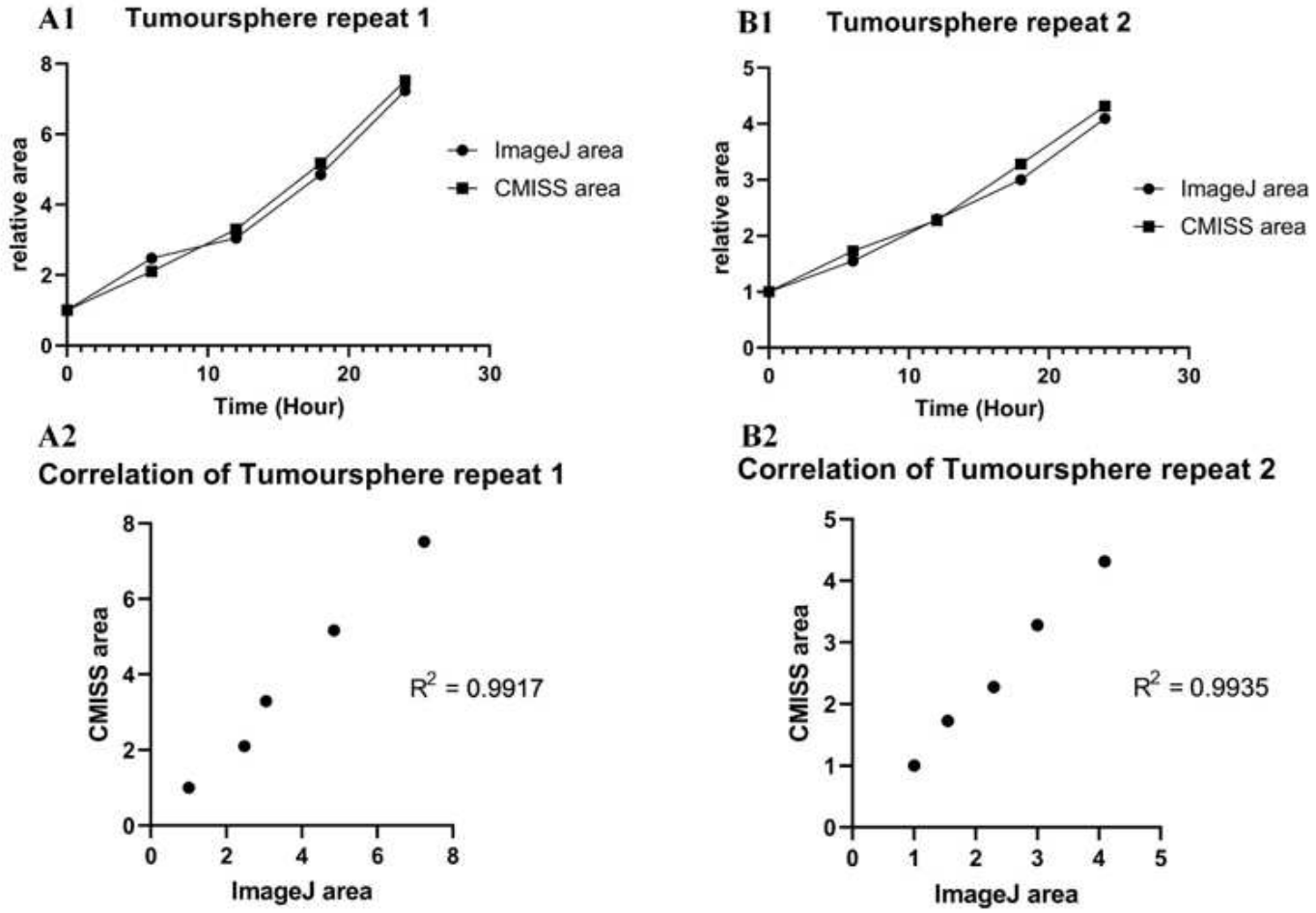

Figure 2

Changes in area measured in ImageJ and FE analysis correlated very highly with each other. Overall area was measured using ImageJ and our FE based method over 24 hours in 6 hour increments on two migrating tumoursphere repeats (A1 and B1). The areas were correlated using the William Pearson Correlation analysis in Graphpad Prism 8 and the R2 was measured (A2 and B2).

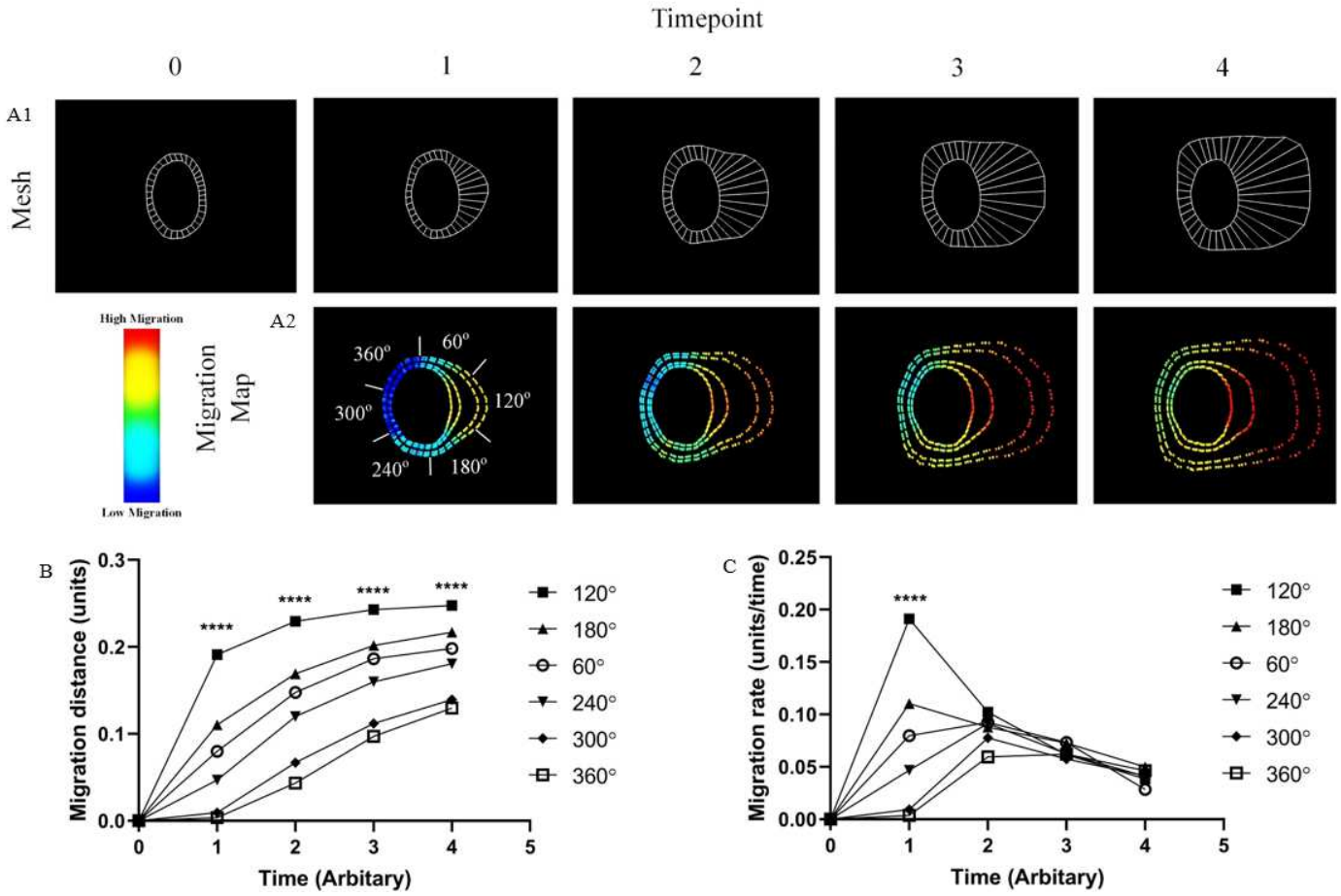

Figure 3

Our FE-based approach accurately quantified regional migration of the phantom data. The phantom data mesh (A1) was utilised in our FE models to quantify the migration rate over time which was visualised in the migration map (Red indicates high migration rate while blue indicates minimal migration rate; A2). Data points in the migration map were segmented in 60˚ increments and averaged, before they were plotted and compared against each other (B). Every segment at each timepoint were compared against the 120˚ segment and statistical significance was assessed via Two-way ANOVA test with Dunnett's post-test; ****p<0.0001 all segments versus 120˚ segment (B). Migration rate was calculated by finding the difference in migration distances between the current timepoint and the previous timepoint, and the difference was divided by the time that has passed between the two timepoints (C).

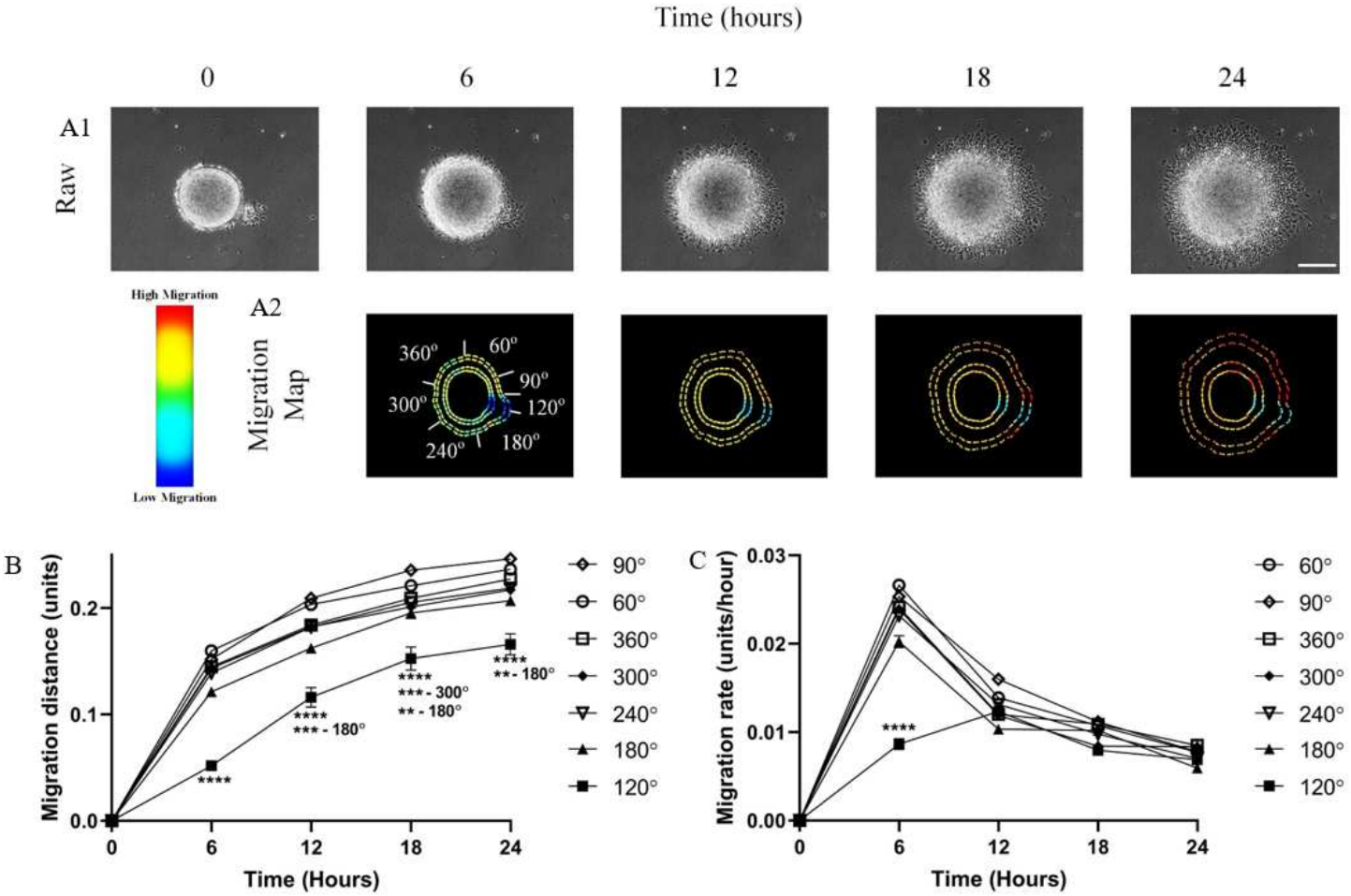

Figure 4

FE-based analysis was capable of detecting and quantifying the nuanced migration. The images of the the migrating tumoursphere were taken every 6 hours for 24 hours (A1) and were analysed by our FE models to produce the migration maps (Red indicates high migration rate while blue indicates minimal migration rate; A2). The data points from the migration maps were plotted and graphed in segments to assess the regional migration of the tumoursphere. Every segment at each timepoint were compared against the 120˚ segment and statistical significance was assessed via Two-way ANOVA test with Dunnett's post-test; **p<0.005, ***p<0.0005, ****p<0.0001 all segments versus 120˚ segment, and different *p from different segment comparisons are outlined in the graph (B). Migration rate was calculated by finding the difference in migration distances between the current timepoint and the previous timepoint, and the difference was divided by the time that has passed between the two timepoints (C). White scale bar represents 250 μm.